

# Ligand centered electrocatalytic efficient CO<sub>2</sub> reduction reaction at low overpotential on single-atom Ni regulated molecular catalyst

Jiazh Wang<sup>1,2</sup>, Qi Hao<sup>1,3</sup>, Haixia Zhong<sup>4</sup>, Kai Li<sup>1</sup>, and Xinbo Zhang<sup>1,2</sup> (✉)<sup>1</sup> State Key Laboratory of Rare Earth Resource Utilization, Changchun Institute of Applied Chemistry, Chinese Academy of Sciences, Changchun 130022, China<sup>2</sup> University of Science and Technology of China, Hefei 230026, China<sup>3</sup> Key Laboratory of Automobile Materials, Ministry of Education, Jilin University, Changchun 130022, China<sup>4</sup> Center for Advancing Electronics Dresden (caed) and Faculty of Chemistry and Food Chemistry, Technische Universität Dresden, Dresden 01062, Germany

© Tsinghua University Press 2022

Received: 9 January 2022 / Revised: 24 January 2022 / Accepted: 25 January 2022

## ABSTRACT

Electrochemical CO<sub>2</sub> reduction reaction (CO<sub>2</sub>RR) into value-added chemicals/fuels is crucial for realizing the sustainable carbon cycle while mitigating the energy crisis. However, it is impeded by the relatively high overpotential and low energy efficiency due to the lack of efficient electrocatalysts. Herein, we develop an isolated single-atom Ni catalyst regulated strategy to activate and stabilize the iron phthalocyanine molecule (Ni SA@FePc) toward a highly efficient CO<sub>2</sub>RR process at low overpotential. The well-defined and homogenous catalytic centers with unique structures confer Ni SA@FePc with a significantly enhanced CO<sub>2</sub>RR performance compared to single-atom Ni catalyst and FePc molecule and afford the atomic understanding on active sites and catalytic mechanism. As expected, Ni SA@FePc exhibits a high selectivity of more significant Faraday efficiency ( $\geq 95\%$ ) over a wide potential range, a high current density of  $\sim 252 \text{ mA}\cdot\text{cm}^{-2}$  at low overpotential (390 mV), and excellent long-term stability for CO<sub>2</sub>RR to CO. X-ray absorption spectroscopy measurement and theoretical calculation indicate the formation of NiN<sub>4</sub>O<sub>2</sub>-FePc heterogeneous structure for Ni SA@FePc. And CO<sub>2</sub>RR prefers to occur at the raised N centers of NiN<sub>4</sub>O<sub>2</sub>-FePc heterogeneous structure for Ni SA@FePc, which enables facilitated adsorption of \*COOH and desorption of CO, and thus accelerated overall reaction kinetics.

## KEYWORDS

single-atom Ni, iron phthalocyanine, molecular catalyst, carbon dioxide reduction reaction, ultra-low overpotential

## 1 Introduction

Electrochemical carbon dioxide reduction reaction (CO<sub>2</sub>RR) into value-added chemicals or fuels, associated with renewable energies, is emerging as a prospective route to close the carbon loop while mitigating relevant environmental and energy crisis [1–3]. For example, CO<sub>2</sub>RR to CO represents one immediate way to realize the sufficient CO<sub>2</sub> conversion for the faster conversion rate compared to the multiple carbon products and the established industrial utilization of CO for high value-added chemicals and fuels. Unfortunately, the inert nature of the CO<sub>2</sub> molecule and the faster competitive hydrogen evolution reaction (HER) bring grand challenges in driving a stable CO<sub>2</sub>RR process with a sufficient current density and high selectivity at low potential [4, 5]. To overcome the above challenges, numerous catalysts have been developed to promote the CO<sub>2</sub>RR process [6–8]. However, simultaneously boosting their activity, selectivity, and stability toward high-efficiency CO<sub>2</sub>RR remains a grand challenge [9]. Meanwhile, the rational design of an effective electrocatalyst for CO<sub>2</sub>RR is hindered by the lack of insightful fundamental study on catalytic site and reaction mechanisms.

To this end, transition metal complex-based molecular catalyst would be one compelling candidate for the high-performance

electrocatalytic CO<sub>2</sub>RR with respect to its uniform and well-defined active sites, maximum atomic utilization, and tunable catalytic structure [10–12]. Considering the well-defined coordination environment, it also offers an ideal platform to unveil the catalytic reaction mechanism. For example, metal phthalocyanine or porphyrin-based molecules on carbon nanotubes have been widely investigated as the most promising molecular catalysts for CO<sub>2</sub>RR [13]. Despite great promise, these molecular catalysts still suffer from low current density, high overpotential, and fast deactivation of catalytic sites. Given that these planar M-N<sub>4</sub> structures of these molecular catalysts can be modulated by the extra coordination with the electron-donating species like O and S groups in axial direction [14], coupling these metal complexes with advanced substrates like functional carbons is expected to be one effective strategy to enhance the activity while stabilizing the active molecules [15]. In this respect, hybrids of the molecular catalyst loaded on a single atom incorporated carbon (M SA/CN) via O linkage are considered as an attractive electrocatalyst for CO<sub>2</sub>RR to CO. This is because: I) The atomically and uniform dispersion of a single atom of the M SA/CN substrate can regulate and stabilize the molecular catalytic center toward high-performance electrocatalysis; II) The

Address correspondence to xbzhang@ciac.ac.cn

TSINGHUA  
UNIVERSITY PRESS

Springer

structural advantages of M SA/CN substrate like good conductivity and the porous structure can be beneficial for sufficient mass/electron transport and large current density [16]; III) The preserved well-defined molecular catalytic sites are favored for gaining depth insights into the reaction mechanism [17–21].

In this work, we develop an isolated single-atom Ni catalyst regulated strategy to activate and stabilize the iron phthalocyanine molecule (Ni SA@FePc) as an effective and selective electrocatalyst for a fast CO<sub>2</sub>RR process at low overpotential. The resultant Ni SA@FePc shows an excellent electrocatalytic CO<sub>2</sub>RR performance regarding its low Tafel slope of 102.7 mV·dec<sup>-1</sup> and large CO partial current density ( $j_{CO}$ ) of ~ 252 mA·cm<sup>-2</sup> at an ultralow overpotential of 0.39 V and outstanding CO selectivity with Faradaic efficiency (FE<sub>CO</sub>) above 95% over a potential range from -0.15 to -0.50 V vs. reference hydrogen electrode (RHE), as well as robust stability for 20 h continuous electrolysis. The extended X-ray absorption fine structures (EXAFS) analysis and theoretical calculations verify the formation of NiN<sub>4</sub>-O<sub>2</sub>-FePc structures for Ni SA@FePc and its contribution to stabilizing the FePc molecule. Density functional theory (DFT) calculations illustrate that such NiN<sub>4</sub>-O<sub>2</sub>-FePc heterogeneous structure will break the symmetric charge distribution of FePc and enable a distinct reduction of the energy barrier for the adsorption of \*COOH, thus resulting in rapid CO<sub>2</sub>RR kinetics on the raised N atoms adjacent to the Fe atom rather than Ni and Fe sites. Our work highlights the potential of regulating and stabilizing the molecular catalysts by single-atom materials for a highly effective strategy to boost efficient electrochemical CO<sub>2</sub>RR and atomic understanding of the catalytic process.

## 2 Experimental

### 2.1 Chemicals

Nickel(II) acetate tetrahydrate (Aladdin, N112914, NiC<sub>4</sub>H<sub>6</sub>O<sub>4</sub>·4H<sub>2</sub>O, 99%), dicyandiamide (Aladdin, D100429, C<sub>2</sub>H<sub>4</sub>N<sub>4</sub>, 98%), 2,2'-bipyridine (Aladdin, D108977, C<sub>10</sub>H<sub>8</sub>N<sub>2</sub>, > 97%), iron(II) phthalocyanine (Aladdin, C<sub>32</sub>H<sub>16</sub>FeN<sub>8</sub>, purified by sublimation, > 98%), potassium bicarbonate (Aladdin, P110485, KHCO<sub>3</sub>, 99.5%), potassium hydroxide (Aladdin, P301749, KOH, 95%), ethanol (Beijing Chemical Works, C<sub>2</sub>H<sub>5</sub>OH, B0301002, ≥ 99.8%), N, N-dimethylformamide (DMF, Aladdin, D119450, C<sub>3</sub>H<sub>7</sub>NO, 99.8%), sulfuric acid (Aldrich, 339741, H<sub>2</sub>SO<sub>4</sub>, 99.999%), hydrochloric acid (Beijing Chemical Works, A0300003, HCl, 35.0%–38.0%), 5% Nafion solution (Dupont, D520), 212 Nafion membrane (Alfa Aesar), and other chemicals were used directly without purification. The water used was ultrapure water.

### 2.2 Instrumentation

Powder X-ray diffraction (PXRD) patterns were obtained from an X-ray diffractometer (micro-XRD, Rigaku, Japan) with Cu K $\alpha$  ( $\lambda = 0.15406$  nm). Scanning electron microscopy (SEM) images were acquired by a field emission scanning electron microscope (Hitachi S4800) operating at an accelerating voltage of 10 kV. Transmission electron microscopy (TEM) images were carried out on a JEM-2100F instrument with a field emission gun operating at 200 kV. High-angle annular dark-field scanning transmission electron microscopy (HAADF-STEM) images and corresponding energy-dispersive spectroscopy mapping were recorded by an FEI Titan Themis 60–300 instrument with a spherical aberration corrector working at 200 kV. Raman spectra were performed on a micro-Raman spectrometer (Renishaw). Fourier transform infrared (FT-IR) spectra were measured at 298 K on a NEXUS-670 spectrometer. X-ray absorption fine structures (XAFS) were

collected on the beamline BL07A1 in NSRRC and were provided technical support by Ceshigo Research Service “www.cephigo.com”. The radiation was monochromatized by a Si (111) double-crystal monochromator. X-ray absorption near-edge structures and extended X-ray absorption fine structures data were processed by Athena software. N<sub>2</sub> adsorption and desorption isotherms were carried out on a Micromeritics ASAP 2020 adsorption analyzer. X-ray photoelectron spectroscopy (XPS) analysis was carried out on a ThermoFisher Scientific ESCALAB 250Xi instrument. All spectra were calibrated according to the C1s binding energy at 284.4 eV. Electrochemical measurements were performed using a Biologic VMP3 electrochemical workstation at room temperature. <sup>1</sup>H nuclear magnetic resonance (NMR) spectra were recorded on Bruker NMR spectrometers (AVANCE-III HD 500). Gas components analysis was performed on ThermoFisher Trace 1300 gas chromatography with pulsed discharge detector (PDD) and flame ionization detector (FID).

### 2.3 Synthesis of Ni SA/CN

Firstly, nickel(II) acetate tetrahydrate (8.5 mg) and 2,2'-bipyridine (12.1 mg) were dissolved in 2 mL of ethanol, and stirred for 2 h at room temperature to obtain a violet solution. Subsequently, carbon substrate synthesized by pyrolyzing sodium citrate tribasic dihydrate (1 g) was added to the above solution and stirred for 12 h. The resulting black paste was dried in an oven at 70 °C for 12 h and then ground with dicyandiamide (100 mg) in a mortar. The mixture was placed in the porcelain and heated at 800 °C under Ar atmosphere for 2 h. The black product was separately washed with HCl, ultrapure water, and ethanol for several times and dried in an oven at 70 °C for 12 h.

### 2.4 Synthesis of Ni SA@FePc

Ni SA@FePc was synthesized via a self-assembly method under liquid conditions. Typically, iron(II) phthalocyanine (3 mg) was first dissolved in 60 mL of DMF by stirring for 6 h under the ambient condition to obtain a dark green solution without further color change. Then, the as-prepared Ni SA/CN (30 mg) was added to the above solution, followed by continuously stirring for 12 h. The solid product was acquired by vacuum filtration and then washed with DMF and ethanol for several times until the supernatant became colorless and transparent. The Ni SA@FePc was harvested by drying in an oven at 60 °C for 12 h.

### 2.5 Synthesis of FePc/C

FePc/C was obtained via a similar method to Ni SA@FePc, except replacing Ni SA/CN with carbon substrate.

### 2.6 Electrochemical measurements

Biologic VMP3 electrochemical workstation was used in all electrochemical measurements under ambient conditions. The evaluations of electrocatalytic CO<sub>2</sub>RR performance were measured in a classical three-electrode H-type cell (separated by Nafion 212 proton exchange membrane) and home-made flow cell (separated by FAA-PK-130 anion exchange membrane) separately. Ag/AgCl electrode was used as a reference electrode. Linear sweep voltammetry (LSV) was measured with a scan rate of 10 mV·s<sup>-1</sup>. The electrochemical impedance spectroscopy (EIS) was performed by applying an alternating current (AC) voltage with the amplitude voltage of 10 mV over a frequency range from 100 kHz to 0.1 Hz. The electrochemical active surface area (ECSA) was evaluated by double-layer capacitance ( $C_{dl}$ ), which was obtained from cyclic voltammetry (CV) results under the potential range of 0.2–0.3 V vs. RHE. The chronoamperometry (CA) tests were conducted at the various potential for 20 min. The gas-phase composition was analyzed on the ThermoFisher Trace 1300

online gas chromatography equipped with PDD and FID detectors. High purity helium (99.9999%) and nitrogen (99.9999%) were employed as a carrier or make-up gas for the chromatography. The liquid products were detected by Bruker AVANCE-III HD 500. All potentials were converted to reversible hydrogen electrodes based on the equation:

$$E_{\text{RHE}} = E_{\text{Ag}/\text{AgCl}} + 0.05916 \times \text{pH} + 0.197 \quad (1)$$

The Faradaic efficiency of the gas product was calculated according to the equation:

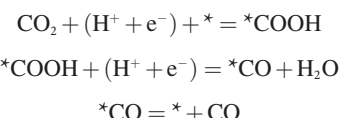
$$\text{FE} = Q_{\text{CO}} / Q_{\text{total}} = Z \times n \times F / Q_{\text{total}} \quad (2)$$

$Q$ : the total charge passed through the working electrode.  $Z$ : the number of transfer electrons, which is 2 for both CO and H<sub>2</sub>.  $n$ : the number of moles for a given product.  $F$ : Faradaic constant (96,485 C·mol<sup>-1</sup>).

## 2.7 Computational details

Vienna *ab initio* simulation package (VASP) based on spin-polarized density functional theory was used for all of the computations. The projector-augmented wave (PAW) method and the generalized gradient approximation (GGA) [22, 23] with the Perdew–Burke–Ernzerhof were used to describe the electron-ion interactions. And a plane-wave energy cutoff was set to 400 eV for structure optimization, and the free energies based on the computational hydrogen electrode (CHE) model proposed by Norskov et al. The Brillouin zone was sampled with the single gamma point k-point set and  $2 \times 2 \times 1$  k-points [24, 25] for electronic structure. Atomic positions were fully relaxed until the forces were less than 0.03 eV·Å<sup>-1</sup> and 10<sup>-5</sup> eV.

The reduction of CO<sub>2</sub> to CO could occur via a pathway by the following steps:



## 3 Results and discussion

### 3.1 Synthesis and characterization of Ni SA@FePc

The synthesis procedure of Ni SA/CN and Ni SA@FePc is shown in Fig. 1(a). Firstly, 2,2'-bipyridine was coordinated with Ni<sup>2+</sup> ion to form a homogeneous Ni-N<sub>4</sub> site without agglomeration during the pyrolysis process for Ni SA/CN. Then, Ni SA@FePc was synthesized via a self-assembly method, wherein the heterostructure of Ni SAs and FePc was formed. For comparison, FePc loaded on carbon substrate (FePc/C) was also synthesized by a similar synthetic process. The SEM, TEM, and high-resolution TEM (HR-TEM) images (Figs. S3 and S4 in the Electronic Supplementary Material (ESM)) show Ni SA/CN, FePc/C, and Ni SA@FePc possess interconnected nanosheets morphology without detectable nanoparticles. Ring-like patterns in selected area electron diffraction (SAED) images (Fig. S3 in the ESM) indicate the amorphous states of Ni SA/CN, FePc/C, and Ni SA@FePc, which are well consistent with X-ray diffraction measurements (Fig. S5 in the ESM), excluding the formation of metallic Ni and Fe. Raman and FT-IR spectra confirm the presence of FePC for both FePc/C and Ni SA@FePc (Fig. S6 in the ESM). To verify the dispersion of Ni and Fe species, HAADF-STEM measurement was carried out. As shown in Fig. 1(d), a large number of bright dots (identified as Ni and Fe atoms) are discovered for Ni SA@FePc, indicating well dispersion of single Ni/Fe atoms on CN substrate [26, 27]. Similarly, the atomic-level dispersed Ni or Fe atoms are also observed in Ni SA/CN and FePc/C samples (Figs. S1 and S2 in the ESM), respectively. The corresponding energy-dispersive X-ray spectroscopy (EDS) images (Fig. 1, Figs. S1, and S2 in the ESM) reveal the uniform distribution of Ni, Fe, N, and O elements over Ni SA/CN, FePc/C, and Ni SA@FePc samples. The according Ni loadings are 0.18 at.% and 0.17 at.% for Ni SA/CN and Ni SA@FePc, while Fe loadings are 0.27 at.% and 0.20 at.% for FePc/C and Ni SA@FePc based on inductively coupled plasma optical emission spectrometry detection (Table S2 in the ESM).

To investigate the fine chemical structures of Ni and Fe sites,

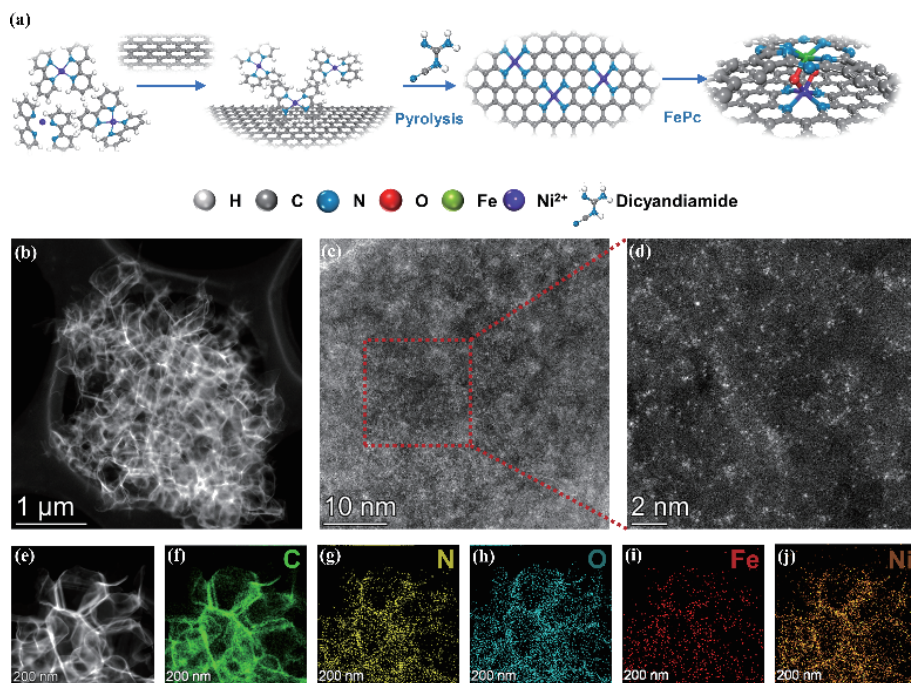


**Figure 1** (a) Schematic illustration of the synthesis for Ni SA/CN and Ni SA@FePc. (b)–(d) HAADF-STEM images for Ni SA@FePc. (e)–(i) Corresponding EDS elemental mapping of Ni SA@FePc.

XANES and EXAFS were acquired by synchrotron XAFS techniques (Fig. 2). The XANES profiles of Fe K-edge for FePc/C and Ni SA@FePc exhibit pre-edge peaks at ~ 7,114 eV for FePc and FePc/C (Fig. 2(a)), which can be discovered due to the symmetric Fe–N<sub>4</sub> sites. The near-edges for FePc/C (~ 7,121 eV) and Ni SA@FePc (~ 7,120 eV) are found between these of Fe foil and Fe<sub>2</sub>O<sub>3</sub>, implying the oxidation states of Fe are between 0 and +3 in both FePc/C and Ni SA@FePc (Fig. 2(b)). Besides, the near-edge of Fe for Ni SA@FePc is located between FePc and FePc/C, in line with the XPS analysis (Fig. S7(a) in the ESM) for Fe 2p<sub>3/2</sub> peaks of Ni SA@FePc (709.4 eV), FePc/C (709.7 eV), and FePc (709.15 eV). The near-edges for Ni SA/CN (~ 8,337 eV) and Ni SA@FePc (~ 8,338 eV) are found between these of Ni foil (8,334 eV) and NiO (8,338 eV) (Fig. 2(d)), implying the oxidation states of Ni are between 0 and +2 in both Ni SA/CN and Ni SA@FePc samples (Fig. 2(e)) [28]. Notably, the near-edge for Ni SA@FePc locates at higher energy compared with Ni SA/CN and thus results in a higher oxidation state of Ni in Ni SA@FePc, which is consistent with the XPS analysis (Fig S7(b) in the ESM). The Ni 2p<sub>3/2</sub> peak of Ni SA@FePc (855.5 eV) appears higher than Ni<sup>0</sup> (852.6 eV) and Ni SA/CN (855.2 eV), further confirming the chemical state of Ni for Ni SA@FePc is higher compared with Ni SA/CN [29]. In addition, both NiPc and Ni SA/CN show pre-edge peaks at ~ 8,334 eV, which can be identified to the planar-shape and highly symmetric Ni–N<sub>x</sub> sites [30]. In contrast, Ni SA@FePc exhibits no pre-edge peak at ~ 8,334 eV, revealing the destruction of symmetric Ni–N<sub>x</sub> structure. Unexpectedly, Ni SA@FePc shows no pre-edge peak, suggesting that the axial coordination destructs the local square-planar structure [31, 32]. The coordination number (CN) of Fe–N/O, Ni–N/O for Ni SA@FePc is 5.5 and 5.8, respectively (Figs. 2(c), 2(f), and Table S1 in the ESM).

The porous structures of the samples were investigated by nitrogen adsorption and desorption isotherms at 77.3 K (Fig. S11 in the ESM). Ni SA@FePc inherits the porous structure of Ni SA/CN, which is beneficial for mass transportation and exposing abundant active sites for CO<sub>2</sub>RR. Besides, Ni SA/CN generates a higher Brunauer–Emmett–Teller (BET) surface area than Ni SA@FePc (Table S3 in the ESM). The slight decrease of

BET surface area for Ni SA@FePc could attribute to the introduction of FePc during the self-assembly process in liquid condition, suggesting the homogeneous distribution of FePc on matrix. The pore diameter distribution curves demonstrate the presence of mesopores and micropores with an average size of 3.749 nm for Ni SA@FePc and 3.331 nm for Ni SA/CN (Table S3 in the ESM). Different N species including Ni/Fe–N, pyrrolic N, pyridinic N, graphic N, and quaternary N are presented in the high-resolution N 1s XPS spectra of Ni SA@FePc and Ni SA/CN (Fig. S8(b) in the ESM), and an obvious increase of Ni/Fe–N in SA@FePc compared with Ni SA/CN could ascribe to the Fe–N bonds in FePc, therefore confirming the coordination of Ni/Fe and N atom in Ni SA@FePc and Ni SA/CN samples. In addition, the increased ratio of Fe–O bonds in Ni SA@FePc compared with that in FePc/C and FePc (Fig. S9(b) in the ESM) reveals extra coordination with Fe–N<sub>4</sub> sites in an axial direction in Ni SA@FePc, in line with the fitting results according to FT EXAFS. The CO<sub>2</sub> absorption properties were measured at 273 K by CO<sub>2</sub> absorption and desorption isotherms. As shown in Fig. S12 in the ESM, Ni SA@FePc acquires higher CO<sub>2</sub> absorption capacity (30.41 cm<sup>3</sup>·g<sup>-1</sup>) than that of Ni SA/CN (22.775 cm<sup>3</sup>·g<sup>-1</sup>) and FePc/C (15.437 cm<sup>3</sup>·g<sup>-1</sup>), which can be owing to its more feasible and accessible absorption sites for CO<sub>2</sub> molecules, and thus favorable for boosting the high catalytic performance.

### 3.2 Electrochemical measurements

The evaluation of electrocatalytic performance for CO<sub>2</sub>RR was first implemented in a classical three-electrode H-type cell (Fig. S13 in the ESM) with 0.1 M KHCO<sub>3</sub>. A significant increase in the current density is observed for Ni SA@FePc when the electrolyte is changed from Ar-saturated to CO<sub>2</sub>-saturated electrolyte, disclosing its more favorable CO<sub>2</sub>RR process than the competing hydrogen evolution reaction (HER) (Fig. S13(a) in the ESM) [33, 34]. Besides, Ni SA@FePc delivers a larger current density and more positive onset potential compared with Ni SA/CN and FePc/C under CO<sub>2</sub>-saturated electrolyte, suggesting the preponderance of Ni SA@FePc for activating CO<sub>2</sub> molecules. Next, CA of CO<sub>2</sub> electrolysis was operated over a potential range from -0.2 to -0.8 V vs. RHE without iR compensation, wherein product

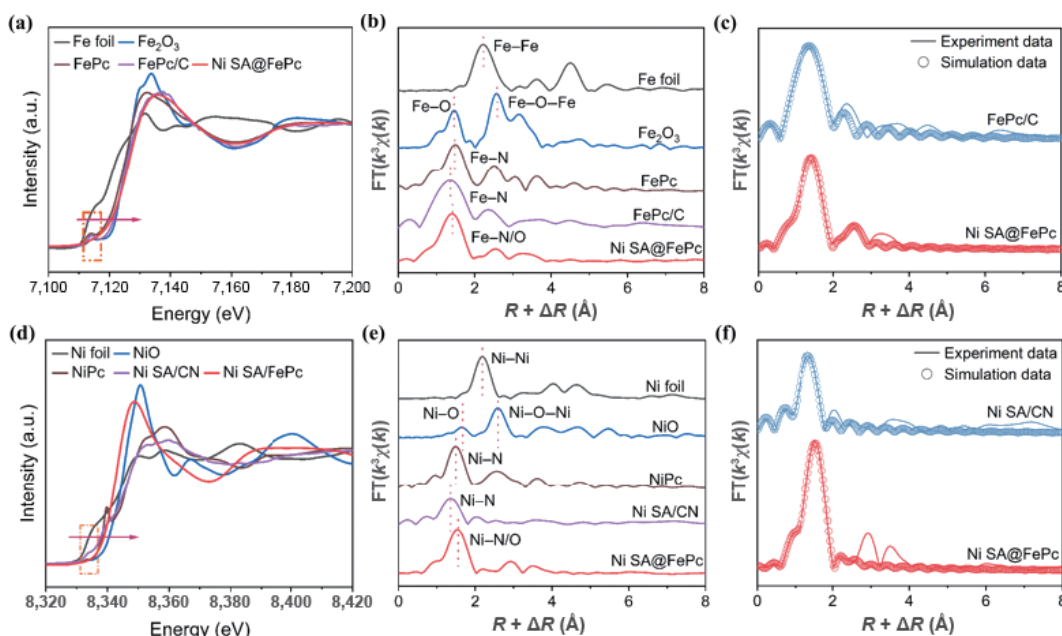


**Figure 2** (a) Fe K-edge XANES profiles of Fe foil, Fe<sub>2</sub>O<sub>3</sub>, FePc, FePc/C, and Ni SA@FePc. (b) Fe K-edge spectra. (c) Fe K-edge FT EXAFS of Ni SA/CN and Ni SA@FePc. (d) Ni K-edge XANES profiles of Ni foil, NiO, NiPc (nickel phthalocyanine), Ni SA/CN, and Ni SA@FePc. (e) Ni K-edge spectra. (f) Ni K-edge FT EXAFS of Ni SA/CN and Ni SA@FePc.

detection was carried out by online gas chromatography (GC) and offline  $^1\text{H}$  NMR. As shown in Figs. S15 and S16 in the ESM, only gas products were detected (CO and  $\text{H}_2$ ) in these catalytic systems. Better behavior of Ni SA@FePc in electrocatalysis  $\text{CO}_2\text{RR}$  to CO is achieved regarding its higher  $\text{FE}_{\text{CO}}$  (Fig. S13(c) in the ESM) and larger  $j_{\text{CO}}$  (Fig. S13(b) in the ESM) than these of Ni SA/CN and FePc/C over the whole applied potentials at  $-0.5$  V vs. RHE. Ni SA@FePc obtains a higher  $\text{FE}_{\text{CO}}$  up to 97.65% than these of Ni SA/CN (95.54%) and FePc/C (95.02%), highlighting its excellent selectivity in electrolysis  $\text{CO}_2$  to CO. Moreover, the feasibility of Ni SA@FePc in practical electrocatalytic  $\text{CO}_2$  to CO is evaluated in a homemade three-electrode flow cell, with catalyst modified gas diffusion layer (GDL) as work electrode and 0.1 M KOH as an electrolyte, which can greatly alleviate the restriction of  $\text{CO}_2$  solubility in a flow cell. Benefiting from this three-phase interface reaction, the CO evolution efficiency is determined by the local catalytic activity of catalysts rather than confined by solubility and diffusion rate. Impressively beneficial from abundant active sites, excellent conductivity, and plentiful pores (Figs. S11 and S12 in the ESM), Ni SA@FePc shows an astonishing  $\text{CO}_2\text{RR}$  performance. As shown in Figs. 3(a)–3(c), Ni SA@FePc displays a large  $j_{\text{CO}}$  ( $\sim 252 \text{ mA}\cdot\text{cm}^{-2}$ ) and high  $\text{FE}_{\text{CO}}$  up to  $\sim 99\%$  at an ultralow overpotential (390 mV), which is 2 fold than these for Ni SA/CN ( $\sim 125 \text{ mA}\cdot\text{cm}^{-2}$ ) and 1.4 fold than FePc/C ( $\sim 175 \text{ mA}\cdot\text{cm}^{-2}$ ), demonstrating the superiority of Ni SA@FePc in electrocatalytic  $\text{CO}_2\text{RR}$  [35]. Besides, the Ni SA@FePc maintains above 95% of FE over the whole applied potential range from  $-0.15$  to  $-0.5$  V vs. RHE. Thus, Ni SA is indeed devoted to activating and stabilizing the molecular FePc

during the  $\text{CO}_2\text{RR}$  process.

Additionally, a lower Tafel slope ( $102.7 \text{ mV}\cdot\text{dec}^{-1}$ , Fig. 3(d)) is obtained by Ni SA@FePc in electrocatalysis  $\text{CO}_2$  to CO compared with Ni SA/CN ( $121.9 \text{ mV}\cdot\text{dec}^{-1}$ ), FePc/C ( $118.8 \text{ mV}\cdot\text{dec}^{-1}$ ), and FePc ( $180.37 \text{ mV}\cdot\text{dec}^{-1}$ ), indicating its faster reaction kinetics and the first electron transfer step for the generation of  $^{*}\text{COOH}$  species as the rate-determining step (RDS) [36]. It is thus clear that Ni SA substrate plays an important role in enhancing the  $\text{CO}_2\text{RR}$  catalytic performance of FePc.

Interestingly, bare FePc exhibits negligible CO current density ( $\sim 1 \text{ mA}\cdot\text{cm}^{-2}$ ) at the whole applied potentials and inferior faradaic efficiency (below 36%), which is consistent with the results using H-type cell ( $j_{\text{CO}} \sim 0.2 \text{ mA}\cdot\text{cm}^{-2}$  and  $\text{FE}_{\text{CO}} \sim 28.8\%$ ). The negligible  $j_{\text{CO}}$  and extremely low  $\text{FE}_{\text{CO}}$  are gained for bare FePc in both H-type cell and flow cell due to its low conductivity, which is confirmed by the EIS analysis (Fig. 3(f)). When supported on a carbon substrate, FePc/C shows obvious improvement in conductivity and thus higher  $j_{\text{CO}}$  and  $\text{FE}_{\text{CO}}$ . However, the  $j_{\text{CO}}$  and  $\text{FE}_{\text{CO}}$  of FePc decay significantly at high potentials (from  $-0.5$  V vs. RHE, Figs. S13 (b) and S13(c) in the ESM), indicating the instability of FePc during the  $\text{CO}_2$  electrolysis process [37, 38]. In sharp contrast,  $j_{\text{CO}}$  and  $\text{FE}_{\text{CO}}$  of Ni SA@FePc maintain even at high potentials. Therefore, despite activating the FePc in accelerating electrocatalysis  $\text{CO}_2\text{RR}$ , Ni SA substrate also contributes to stabilizing the molecular catalytic centers of Ni SA@FePc.

The electrochemical capacitance measurements were also implemented to evaluate the ECSA by acquiring the  $C_{\text{dl}}$  as reference (Fig. 3(e) and Fig. S20 in the ESM). Ni SA@FePc shows

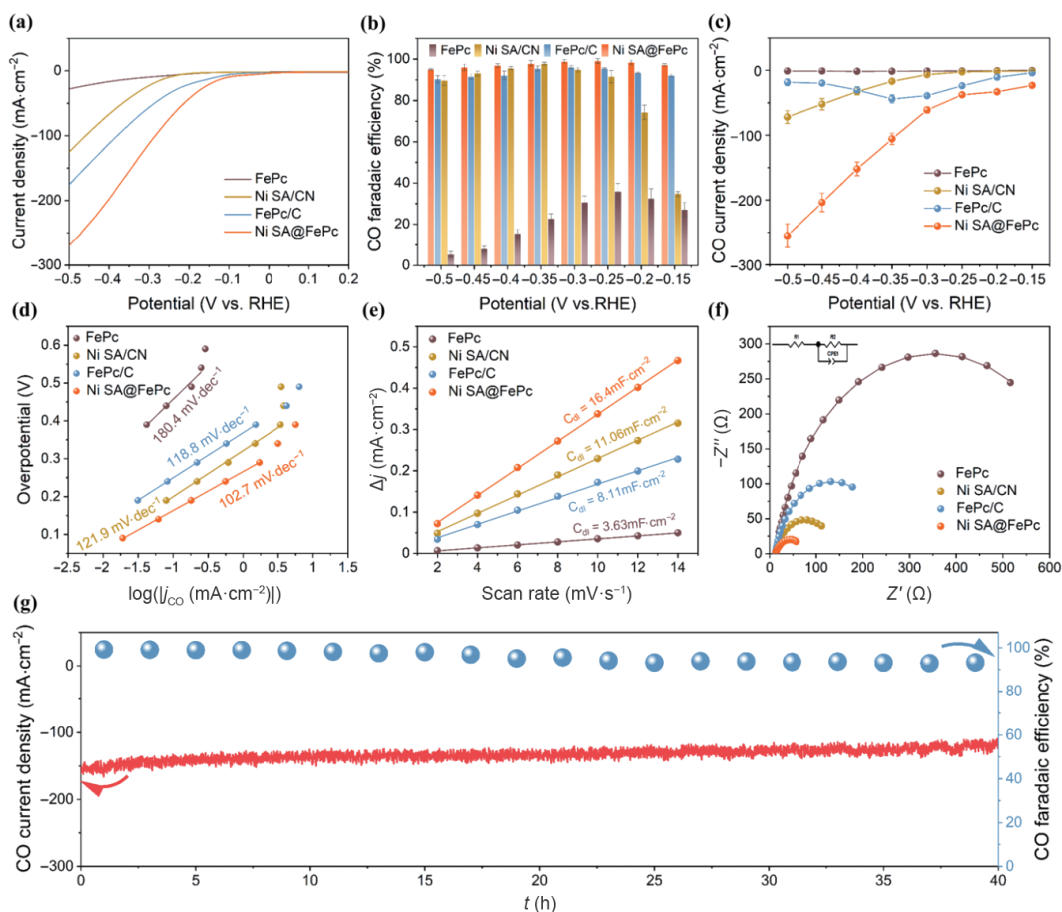


**Figure 3** (a) Linear sweep voltammetry curves of FePc, Ni SA/CN, FePc/C, and Ni SA@FePc under  $\text{CO}_2$  gas flow in 0.1 M KOH electrolyte with home-made flow cell. (b) CO Faradaic efficiency for FePc, Ni SA/CN, FePc/C, and Ni SA@FePc. (c) CO current density for FePc, Ni SA/CN, FePc/C, and Ni SA@FePc. (d) Tafel slopes of FePc, Ni SA/CN, FePc/C, and Ni SA@FePc. (e) Double layer capacity and (f) Nyquist plots for FePc, Ni SA/CN, FePc/C, and Ni SA@FePc. (g) Long-term electrolysis of Ni SA@FePc at  $-0.4$  V vs. RHE.

a much higher normalized  $C_{dl}$  of  $16.4 \text{ mF}\cdot\text{cm}^{-2}$  than these of FePc ( $3.63 \text{ mF}\cdot\text{cm}^{-2}$ ), Ni SA/CN ( $11.06 \text{ mF}\cdot\text{cm}^{-2}$ ), and FePc/C ( $8.11 \text{ mF}\cdot\text{cm}^{-2}$ ) that Ni SA@FePc possesses significant larger ECSA, which is favorable for exposing more electrochemical active sites [39]. Besides, Ni SA@FePc also shows elevated electron transfer kinetic during the  $\text{CO}_2\text{RR}$  process compared with Ni SA/CN and FePc/C as it demonstrates lower charge transfer resistance based on the Nyquist plots (Fig. 3(f)), illustrating the more facilitated pathway to conduct charges for enhancing  $\text{CO}_2$  adsorption and activation to achieve the purpose of CO evolution on Ni SA@FePc. Thereby, Ni SA@FePc with a high density of active sites, large specific surface area, and high conductivity has incomparable superiority in electrocatalytic  $\text{CO}_2$  to CO compared with Ni SA/CN and FePc/C.

The long-term stability in the flow cell was examined at  $-0.4 \text{ V}$  vs. RHE in  $0.1 \text{ M KOH}$  electrolyte. As shown in Fig. 3(g), only slight attenuation of  $j_{\text{CO}}$  ( $\sim 150 \text{ mA}\cdot\text{cm}^{-2}$ ) with  $\text{FE}_{\text{CO}}$  above 90% under 20 h uninterrupted electrolysis is observed for Ni SA@FePc, elucidating the preeminent stability and superior selectivity of catalytic sites for  $\text{CO}_2$  reduction under large current density condition. Besides, long-time durability of Ni SA@FePc (Fig. S13(d) in the ESM) in an H-type cell is also tested, and no apparent degradation of current density ( $\sim 18 \text{ mA}\cdot\text{cm}^{-2}$ ) under 20 h continuous electrocatalysis at  $-0.7 \text{ V}$  vs. RHE. The slight decay of CO faradaic efficiency ( $\sim 97\%$  to  $91\%$ ) likely originates from the carbonate accumulation on the surface of the electrode, which could cover up the active sites. The ex-situ XRD (Fig. S17 in the ESM), UV-vis spectra (Fig. S18 in the ESM), and XPS analysis (Fig. S19 in the ESM) exclude the generation of metallic Ni/Fe phases in Ni SA@FePc sample after 20 h electrolysis. It is thus concluded that the stable molecular heterogeneous structure of Ni SA@FePc with inherited advantages of single Ni atom sites and molecular FePc, as well as new regulated catalytic centers, demonstrating excellent feasibility in electrocatalysis  $\text{CO}_2\text{RR}$  to CO.

### 3.3 DFT calculations

To understand the underlying catalytic mechanism for  $\text{CO}_2$  activation and reduction, DFT calculations were performed to construct appropriate models in line with XAFS results and illustrate the real active sites on theoretical sights [40]. According to the fitting data of EXAFS, the ideal models of Ni SA@FePc were built with  $\text{NiN}_4\text{-O}_2\text{-FePc}$  three-dimensional structure shown in Fig. S23 in the ESM, denoted as model 1 named  $\text{NiN}_4\text{-O}_2\text{-FePc-1}$  (Fig. S23(b) in the ESM), model 2 named  $\text{NiN}_4\text{-O}_2\text{-FePc-2}$  (Fig. S23(c) in the ESM), and model 3 named  $\text{NiN}_4\text{-O}_2\text{-FePc-3}$  (Fig. S23(d) in the ESM), respectively, in which a concave  $\text{Fe-N}_4$  center was formed due to the axial stretching by oxygen atoms. Meanwhile, a raised  $\text{Ni-N}_4$  (defined as model 5 named  $\text{NiN}_4$ ) coordination environment was also appeared by interacting with oxygen atoms. The introduction of oxygen atoms bridge Ni and Fe species and break the in-plane metal- $\text{N}_4$  centers, confirmed by XANES profiles. Besides, the model of Ni SA/CN (Fig. 4(b) and Fig. S21(a) in the ESM) was established with  $\text{Ni-N}_4$  coordination structures embedded in graphene and FePc/C (defined as model 4 named FePc/C as shown in Fig. 4(c) and Fig. S22(a) in the ESM) was considered as a graphene-FePc double-layer structure, interacting with Van der Waals force. Herein we put forward three models of Ni SA@FePc to verify the reaction site for  $\text{CO}_2\text{RR}$  (Fig. 4) because of the novel concave structure. As shown in Fig 4(a), model 2 ( $\text{NiN}_4\text{-O}_2\text{-FePc-2}$ , Fig. 4(e) and Fig. S23(c) in the ESM) exhibits lowest energy barrier for the adsorption of  ${}^*\text{COOH}$  ( $0.01 \text{ eV}$ ) compared with model 1 ( $\text{NiN}_4\text{-O}_2\text{-FePc-1}$ ,  $2.06 \text{ eV}$ , Fig. 4(d) and Fig. S23(b) in the ESM), model 3 ( $\text{NiN}_4\text{-O}_2\text{-FePc-3}$ ,

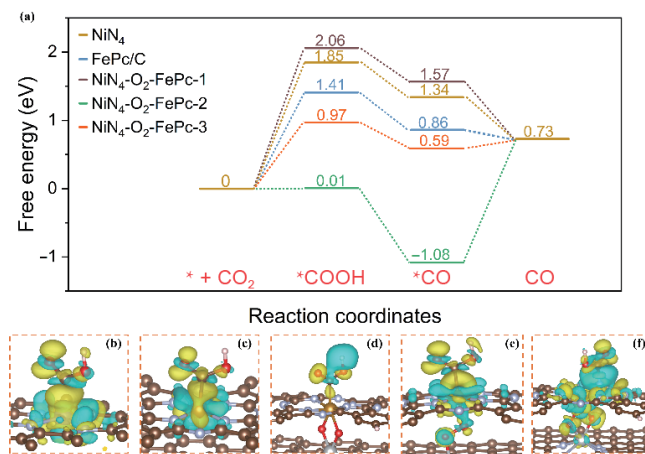


**Figure 4** (a) The Gibbs free energy plots of  $\text{CO}_2\text{RR}$  on different models. Inset: adsorption configurations of  ${}^*\text{COOH}$  on a different surface. (b)–(f) Corresponding charge density difference plots for different models.

$0.97 \text{ eV}$ , Fig. 4(f) and Fig. S23(d) in the ESM), model 4 (FePc/C,  $1.41 \text{ eV}$ , Fig. S22(a) in the ESM), and model 5 ( $\text{NiN}_4$ ,  $1.85 \text{ eV}$ , Fig. S21(a) in the ESM).

Charge density difference plots (Figs. 4(b)–4(f)) illustrate that, upon the adsorption of  ${}^*\text{COOH}$ , model 1 shows that there is less electronic interaction between COOH and Fe, suggesting that weakest adsorption for  ${}^*\text{COOH}$ . In contrast, the adsorption center of model 2 is pentacoordinate Fe site, where electrons could be provided to  ${}^*\text{COOH}$  and strengthen the interaction between  ${}^*\text{COOH}$  and Fe site, resulting in difficult desorption of CO [41]. Differently, model 3 manifests a moderate energy barrier for  ${}^*\text{COOH}$  adsorption and spontaneous desorption for  ${}^*\text{CO}$ , indicating an RDS of  ${}^*\text{COOH}$  adsorption, consistent with the results based on Tafel slopes analysis. The Fe site with hex coordinate environment owns inferior charge distribution and adsorption of  ${}^*\text{COOH}$ , illustrating its inapplicability as an active site. Besides, the strong interaction of Fe and O atoms result in the reconstruction of FePc and the stretch of Fe-N bonds, which motivates the catalytic activity and increases the charge distribution. Importantly, such transformation promotes the adsorption for  ${}^*\text{COOH}$  on N atoms next to Fe atoms. It also enables a spontaneous step for  ${}^*\text{CO}$  desorption and the obviously improved catalytic performance along with activating more N active sites by sacrificing Fe sites, accounting for the high  $\text{CO}_2\text{RR}$  performance in a flow cell on Ni SA@FePc (Fig. 3).

## 4 Conclusion

In summary, we have developed a single atom Ni regulated FePc molecular catalyst (Ni SA@FePc) and achieved a great enhancement in electrocatalytic  $\text{CO}_2\text{RR}$  along with a satisfying CO selectivity with more than 90% CO Faradaic efficiency in a wide potential window (from  $-0.2 \text{ V}$  to  $-0.8 \text{ V}$  vs. RHE), high current density ( $\sim 252 \text{ mA}\cdot\text{cm}^{-2}$ ) at a low overpotential ( $390 \text{ mV}$ ) and long-term stability (20 h) in alkaline electrolyte. Combining XAFS techniques and DFT calculations, we propose an original concave  $\text{Fe-N}_4$  and raised  $\text{Ni-N}_4$  three-dimension heterogenous structure for Ni SA@FePc, which are bridged by two O atoms. Besides, the interaction between Ni and Fe species further stabilizes the unstable FePc molecules and provides new active sites (the N atom next to Fe atom) for  $\text{CO}_2\text{RR}$ , in line with the evaluation of  $\text{CO}_2\text{RR}$ , respectively. This regulation strategy illustrates a prospective avenue in pursuing atomic-level motifs for highly efficient electrocatalysis by regulating the coordination of the catalytic centers and speeding up the fundamental studies in catalytic mechanisms.

## Acknowledgments

H. X. Z. acknowledges funding from the Alexander von Humboldt Foundation. This work was supported by the National Natural Science Foundation of China (No. 21725103), National Key R&D Program of China (No. 2019YFA0705704), the Strategic Priority Research Program of the Chinese Academy of Sciences (No. XDA21010210), Jilin Province Science and Technology Development Plan Funding Project (No. 20200201079JC), Changchun Science and Technology Development Plan Funding Project (No. 19SS010), Jilin Province Capital Construction Funds Project (No. 2020C026-1), and the K. C. Wong Education Foundation (No. GJTD-2018-09).

**Electronic Supplementary Material:** Supplementary material (TEM, HR-TEM, HAADF-STEM, XRD, FT-IR, Raman, XPS, <sup>1</sup>H-NMR, UV-Vis, electrochemical capacitance, and DFT models) is available in the online version of this article at <https://dx.doi.org/10.1007/s12274-022-4197-6>.

## References

- [1] Chu, S.; Cui, Y.; Liu, N. The path towards sustainable energy. *Nat. Mater.* **2017**, *16*, 16–22.
- [2] Mitchell, S.; Pérez-Ramírez, J. Single atom catalysis: A decade of stunning progress and the promise for a bright future. *Nat. Commun.* **2020**, *11*, 4302.
- [3] Obama, B. The irreversible momentum of clean energy. *Science* **2017**, *355*, 126–129.
- [4] Gu, J.; Hsu, C. S.; Bai, L. C.; Chen, H. M.; Hu, X. L. Atomically dispersed Fe<sup>3+</sup> sites catalyze efficient CO<sub>2</sub> electroreduction to CO. *Science* **2019**, *364*, 1091–1094.
- [5] Zheng, T. T.; Jiang, K.; Ta, N.; Hu, Y. F.; Zeng, J.; Liu, J. Y.; Wang, H. T. Large-scale and highly selective CO<sub>2</sub> electrocatalytic reduction on nickel single-atom catalyst. *Joule* **2019**, *3*, 265–278.
- [6] Wu, Y. S.; Jiang, Z.; Lu, X.; Liang, Y. Y.; Wang, H. L. Domino electroreduction of CO<sub>2</sub> to methanol on a molecular catalyst. *Nature* **2019**, *575*, 639–642.
- [7] Wang, Y. C.; Xu, L.; Zhan, L. S.; Yang, P. Y.; Tang, S. H.; Liu, M. J.; Zhao, X.; Xiong, Y.; Chen, Z. Y.; Lei, Y. H. Electron accumulation enables Bi efficient CO<sub>2</sub> reduction for formate production to boost clean Zn-CO<sub>2</sub> batteries. *Nano Energy* **2022**, *92*, 106780.
- [8] Zhang, X.; Wu, Z. S.; Zhang, X.; Li, L. W.; Li, Y. Y.; Xu, H. M.; Li, X. X.; Yu, X. L.; Zhang, Z. S.; Liang, Y. Y. et al. Highly selective and active CO<sub>2</sub> reduction electrocatalysts based on cobalt phthalocyanine/carbon nanotube hybrid structures. *Nat. Commun.* **2017**, *8*, 14675.
- [9] Zhong, M.; Tran, K.; Min, Y. M.; Wang, C. H.; Wang, Z. Y.; Dinh, C. T.; De Luna, P.; Yu, Z. Q.; Rasouli, A. S.; Brodersen, P. et al. Accelerated discovery of CO<sub>2</sub> electrocatalysts using active machine learning. *Nature* **2020**, *581*, 178–183.
- [10] Ju, W.; Bagger, A.; Hao, G. P.; Varela, A. S.; Sinev, I.; Bon, V.; Roldan Cuanya, B.; Kaskel, S.; Rossmeisl, J.; Strasser, P. Understanding activity and selectivity of metal-nitrogen-doped carbon catalysts for electrochemical reduction of CO<sub>2</sub>. *Nat. Commun.* **2017**, *8*, 944.
- [11] Zhang, T. Y.; Han, X.; Yang, H. B.; Han, A. J.; Hu, E. Y.; Li, Y. P.; Yang, X. Q.; Wang, L.; Liu, J. F.; Liu, B. Atomically dispersed nickel(I) on an alloy-encapsulated nitrogen-doped carbon nanotube array for high-performance electrochemical CO<sub>2</sub> reduction reaction. *Angew. Chem., Int. Ed.* **2020**, *59*, 12055–12061.
- [12] Chen, K. J.; Liu, K.; An, P. D.; Li, H. J. W.; Lin, Y. Y.; Hu, J. H.; Jia, C. K.; Fu, J. W.; Li, H. M.; Liu, H. et al. Iron phthalocyanine with coordination induced electronic localization to boost oxygen reduction reaction. *Nat. Commun.* **2020**, *11*, 4173.
- [13] Zhang, X.; Wang, Y.; Gu, M.; Wang, M. Y.; Zhang, Z. S.; Pan, W. Y.; Jiang, Z.; Zheng, H. Z.; Lucero, M.; Wang, H. L. et al. Molecular engineering of dispersed nickel phthalocyanines on carbon nanotubes for selective CO<sub>2</sub> reduction. *Nat. Energy* **2020**, *5*, 684–692.
- [14] Hou, Y.; Qiu, M.; Kim, M. G.; Liu, P.; Nam, G.; Zhang, T.; Zhuang, X. D.; Yang, B.; Cho, J.; Chen, M. W. et al. Atomically dispersed nickel-nitrogen-sulfur species anchored on porous carbon nanosheets for efficient water oxidation. *Nat. Commun.* **2019**, *10*, 1392.
- [15] Sun, X. H.; Tuo, Y. X.; Ye, C. L.; Chen, C.; Lu, Q.; Li, G. N.; Jiang, P.; Chen, S. H.; Zhu, P.; Ma, M. et al. Phosphorus induced electron localization of single iron sites for boosted CO<sub>2</sub> electroreduction reaction. *Angew. Chem., Int. Ed.* **2021**, *60*, 23614–23618.
- [16] Yang, H. B.; Hung, S. F.; Liu, S.; Yuan, K. D.; Miao, S.; Zhang, L. P.; Huang, X.; Wang, H. Y.; Cai, W. Z.; Chen, R. et al. Atomically dispersed Ni(I) as the active site for electrochemical CO<sub>2</sub> reduction. *Nat. Energy* **2018**, *3*, 140–147.
- [17] Jiang, K.; Siahrostami, S.; Zheng, T. T.; Hu, Y. F.; Hwang, S.; Stavitski, E.; Peng, Y. D.; Dynes, J.; Gangisetty, M.; Su, D. et al. Isolated Ni single atoms in graphene nanosheets for high-performance CO<sub>2</sub> reduction. *Energy Environ. Sci.* **2018**, *11*, 893–903.
- [18] Jiang, Z. L.; Wang, T.; Pei, J. J.; Shang, H. S.; Zhou, D. N.; Li, H. J.; Dong, J. C.; Wang, Y.; Cao, R.; Zhuang, Z. B. et al. Discovery of main group single Sb-N<sub>4</sub> active sites for CO<sub>2</sub> electroreduction to formate with high efficiency. *Energy Environ. Sci.* **2020**, *13*, 2856–2863.
- [19] Lin, L.; Li, H. B.; Yan, C. C.; Li, H. F.; Si, R.; Li, M. R.; Xiao, J. P.; Wang, G. X.; Bao, X. H. Synergistic catalysis over iron-nitrogen sites anchored with cobalt phthalocyanine for efficient CO<sub>2</sub> electroreduction. *Adv. Mater.* **2019**, *31*, 1903470.
- [20] Ren, S. X.; Joulié, D.; Salvatore, D.; Torbensen, K.; Wang, M.; Robert, M.; Berlinguet, C. P. Molecular electrocatalysts can mediate fast, selective CO<sub>2</sub> reduction in a flow cell. *Science* **2019**, *365*, 367–369.
- [21] Ren, W. H.; Tan, X.; Yang, W. F.; Jia, C.; Xu, S. M.; Wang, K. X.; Smith, S. C.; Zhao, C. Isolated diatomic Ni-Fe metal-nitrogen sites for synergistic electroreduction of CO<sub>2</sub>. *Angew. Chem., Int. Ed.* **2019**, *58*, 6972–6976.
- [22] Blöchl, P. E. Projector augmented-wave method. *Phys. Rev. B* **1994**, *50*, 17953–17979.
- [23] Perdew, J. P.; Burke, K.; Ernzerhof, M. Generalized gradient approximation made simple. *Phys. Rev. Lett.* **1996**, *77*, 3865–3868.
- [24] Wang, V.; Xu, N.; Liu, J. C.; Tang, G.; Geng, W. T. VASPKIT: A user-friendly interface facilitating high-throughput computing and analysis using VASP code. *Comput. Phys. Commun.* **2021**, *267*, 108033.
- [25] Jing, H. Y.; Zhu, P.; Zheng, X. B.; Zhang, Z. D.; Wang, D. S.; Li, Y. D. Theory-oriented screening and discovery of advanced energy transformation materials in electrocatalysis. *Adv. Powder Mater.* **2021**, *100013*.
- [26] Zhou, H.; Yang, T.; Kou, Z. K.; Shen, L.; Zhao, Y. F.; Wang, Z. Y.; Wang, X. Q.; Yang, Z. K.; Du, J. Y.; Xu, J. et al. Negative pressure pyrolysis induced highly accessible single sites dispersed on 3D graphene frameworks for enhanced oxygen reduction. *Angew. Chem., Int. Ed.* **2020**, *59*, 20465–20469.
- [27] Zhu, Z. J.; Yin, H. J.; Wang, Y.; Chuang, C. H.; Xing, L.; Dong, M. Y.; Lu, Y. R.; Casillas-Garcia, G.; Zheng, Y. L.; Chen, S. et al. Coexisting single-atomic Fe and Ni sites on hierarchically ordered porous carbon as a highly efficient ORR electrocatalyst. *Adv. Mater.* **2020**, *32*, 2004670.
- [28] Yang, H. P.; Lin, Q.; Zhang, C.; Yu, X. Y.; Cheng, Z.; Li, G. D.; Hu, Q.; Ren, X. Z.; Zhang, Q. L.; Liu, J. H. et al. Carbon dioxide electroreduction on single-atom nickel decorated carbon membranes with industry compatible current densities. *Nat. Commun.* **2020**, *11*, 593.
- [29] Chen, Y. J.; Gao, R.; Ji, S. F.; Li, H. J.; Tang, K.; Jiang, P.; Hu, H. B.; Zhang, Z. D.; Hao, H. G.; Qu, Q. Y. et al. Atomic-level modulation of electronic density at cobalt single-atom sites derived from metal-organic frameworks: Enhanced oxygen reduction performance. *Angew. Chem., Int. Ed.* **2021**, *60*, 3212–3221.
- [30] Yang, Q. H.; Yang, C. C.; Lin, C. H.; Jiang, H. L. Metal-organic

- framework-derived hollow N-doped porous carbon with ultrahigh concentrations of single Zn atoms for efficient carbon dioxide conversion. *Angew. Chem., Int. Ed.* **2019**, *58*, 3511–3515.
- [31] Zhang, B. X.; Zhang, J. L.; Shi, J. B.; Tan, D. X.; Liu, L. F.; Zhang, F. Y.; Lu, C.; Su, Z. Z.; Tan, X. N.; Cheng, X. Y. et al. Manganese acting as a high-performance heterogeneous electrocatalyst in carbon dioxide reduction. *Nat. Commun.* **2019**, *10*, 2980.
- [32] Luo, F.; Roy, A.; Silvioli, L.; Cullen, D. A.; Zitolo, A.; Sougrati, M. T.; Oguz, I. C.; Mineva, T.; Teschner, D.; Wagner, S. et al. P-block single-metal-site tin/nitrogen-doped carbon fuel cell cathode catalyst for oxygen reduction reaction. *Nat. Mater.* **2020**, *19*, 1215–1223.
- [33] Zang, W. J.; Sun, T.; Yang, T.; Xi, S. B.; Waqar, M.; Kou, Z. K.; Lyu, Z.; Feng, Y. P.; Wang, J.; Pennycook, S. J. Efficient hydrogen evolution of oxidized Ni–N<sub>3</sub> defective sites for alkaline freshwater and seawater electrolysis. *Adv. Mater.* **2021**, *33*, 2003846.
- [34] Yan, C. C.; Li, H. B.; Ye, Y. F.; Wu, H. H.; Cai, F.; Si, R.; Xiao, J. P.; Miao, S.; Xie, S. H.; Yang, F. et al. Coordinatively unsaturated nickel-nitrogen sites towards selective and high-rate CO<sub>2</sub> electroreduction. *Energy Environ. Sci.* **2018**, *11*, 1204–1210.
- [35] Voiry, D.; Shin, H. S.; Loh, K. P.; Chhowalla, M. Low-dimensional catalysts for hydrogen evolution and CO<sub>2</sub> reduction. *Nat. Rev. Chem.* **2018**, *2*, 0105.
- [36] Kong, X. D.; Ke, J. W.; Wang, Z. Q.; Liu, Y.; Wang, Y. B.; Zhou, W. R.; Yang, Z. W.; Yan, W. S.; Geng, Z. G.; Zeng, J. Co-based molecular catalysts for efficient CO<sub>2</sub> reduction via regulating spin states. *Appl. Catal. B: Environ.* **2021**, *290*, 120067.
- [37] Liu, X.; Jiao, Y.; Zheng, Y.; Jaroniec, M.; Qiao, S. Z. Building up a picture of the electrocatalytic nitrogen reduction activity of transition metal single-atom catalysts. *J. Am. Chem. Soc.* **2019**, *141*, 9664–9672.
- [38] Bénisvy, L.; Halut, S.; Donnadieu, B.; Tuchagues, J. P.; Chottard, J. C.; Li, Y. Monomeric iron(II) hydroxo and iron(III) dihydroxo complexes stabilized by intermolecular hydrogen bonding. *Inorg. Chem.* **2006**, *45*, 2403–2405.
- [39] Hikichi, S.; Ogihara, T.; Fujisawa, K.; Kitajima, N.; Akita, M.; Moro-Oka, Y. Synthesis and characterization of the benzoylformato ferrous complexes with the hindered tris(pyrazolyl)borate ligand as a structural model for mononuclear non-heme iron enzymes. *Inorg. Chem.* **1997**, *36*, 4539–4547.
- [40] Chen, S. H.; Li, W. H.; Jiang, W. J.; Yang, J. R.; Zhu, J. X.; Wang, L. Q.; Ou, H. H.; Zhuang, Z. C.; Chen, M. Z.; Sun, X. H. et al. MOF encapsulating N-heterocyclic carbene-ligated copper single-atom site catalyst towards efficient methane electrosynthesis. *Angew. Chem., Int. Ed.* **2022**, *61*, e202114450.
- [41] Wang, Y. N.; Zheng, Y.; Han, C.; Chen, W. Surface charge transfer doping for two-dimensional semiconductor-based electronic and optoelectronic devices. *Nano Res.* **2021**, *14*, 1682–1697.